Candidates for a possible third-generation gravitational wave detector: comparison of ring-Sagnac and sloshing-Sagnac speedmeter interferometers

2017 Class. Quantum Grav. 34 024001

(http://iopscience.iop.org/0264-9381/34/2/024001)

OPEN ACCESS
IOP Publishing
Classical and Quantum Gravity
Class. Quantum Grav. **34** (2017) 024001 (19pp)
doi:10.1088/1361-6382/34/2/024001

Candidates for a possible third-generation gravitational wave detector: comparison of ring-Sagnac and sloshing-Sagnac speedmeter interferometers

S H Huttner, S L Danilishin, B W Barr, A S Bell, C Gräf, J S Hennig, S Hild, E A Houston, S S Leavey, D Pascucci, B Sorazu, A P Spencer, S Steinlechner, J L Wright, T Zhang and K A Strain

SUPA, School of Physics and Astronomy, University of Glasgow, Glasgow G12 8QQ, UK

E-mail: sabina.huttner@glasgow.ac.uk

Received 16 June 2016, revised 1 November 2016
Accepted for publication 22 November 2016
Published 20 December 2016

Abstract

Speedmeters are known to be quantum non-demolition devices and, by potentially providing sensitivity beyond the standard quantum limit, become interesting for third generation gravitational wave detectors. Here we introduce a new configuration, the sloshing-Sagnac interferometer, and compare it to the more established ring-Sagnac interferometer. The sloshing-Sagnac interferometer is designed to provide improved quantum noise limited sensitivity and lower coating thermal noise than standard position meter interferometers employed in current gravitational wave detectors. We compare the quantum noise limited sensitivity of the ring-Sagnac and the sloshing-Sagnac interferometers, in the frequency range, from 5 Hz to 100 Hz, where they provide the greatest potential benefit. We evaluate the improvement in terms of the unweighted noise reduction below the standard quantum limit, and by finding the range up to which binary black hole inspirals may be observed. The sloshing-Sagnac was found to give approximately similar or better sensitivity than the ring-Sagnac in all cases. We also show that by eliminating the requirement for maximally-reflecting cavity end mirrors with correspondingly-thick multi-layer coatings, coating noise can be reduced by a factor of approximately 2.2 compared to conventional interferometers.

Keywords: interferometer, speedmeter, gravitational wave detector

(Some figures may appear in colour only in the online journal)

1. Introduction

The most sensitive position-sensing interferometers [1–3] are predicted to closely approach the standard quantum limit (SQL) within the next few years and will be limited by quantum noise over much of the observing band [4]. This motivates the application of quantum non-demolition (QND) measurements as a route to further improvements in sensitivity, by reducing the quantum noise, for so-called third-generation detectors such as the Einstein telescope (ET) [5].

Two broad classes of QND interferometers have received extensive consideration. One approach exploits quantum noise correlations introduced as a result of opto-mechanical interactions within the interferometer, and further manipulates these correlations using techniques such as filter cavities to obtain improved spectra of quantum noise [7]. The other approach, which is the subject of this paper, is the speedmeter [6]. It has been shown that an *ideal* speedmeter, measuring velocity as a surrogate for canonical momentum and with no sensitivity to the positions of its components, has no quantum back-action noise. The sensitivity of such an instrument would be limited solely by photon-counting (or shot) noise. The relevant theory of speedmeters is introduced in section 2. It is anticipated that a combination of technical and fundamental differences in performance will promote one or other of these designs for application in the gravitational wave detectors of the future.

Several speedmeter topologies have been discovered. All of the methods identified involve eliminating the position information by cancelling or 'subtracting' two sequential position measurements carried out at times separated by an interval governed by the light storage time of the optical cavities in the interferometer arms. Their design is optimised to give the best signal response in the gravitational wave band targeted by the instrument. Quantum back-action, in the form of quantum radiation pressure noise limits the low-frequency performance of conventional instruments, typically below approximately 100 Hz. This is therefore the band targeted by speedmeter designs.

The process of optical subtraction occurs naturally in a Sagnac interferometer [8] but can also be arranged to occur in Michelson-based designs. To achieve this, signal-carrying light is stored for a short period after which it is combined with signal-containing light from a later time such that position information cancels. The process of storing the light and feeding it back into the system with the appropriate time delay (or phase shift) is called 'sloshing'. One design has linear Fabry–Pérot (FP) cavities and employs polarising optics [9, 11, 12], while a second has FP cavities in the interferometer arms and has an additional sloshing cavity to store the light for the chosen time [11–15]. Sloshing systems can also be built around configurations with ring cavities in the arms [8].

Experiment lags considerably behind the theoretical efforts in this area: there have been two tabletop experiments [16, 17] and, at the present moment, construction of the first fully suspended Sagnac interferometer is underway [18]. In order to develop a design suitable for deployment in future long-baseline gravitational wave detectors, it is necessary to combine theory, modelling and experiment to identify the system which offers the best balance of performance and practicality. The present work aims to take forward the modelling phase in preparation for experimental work.

In this paper we compare the two currently-known Sagnac-based configurations, namely the ring-Sagnac interferometer (RSI) and the sloshing-Sagnac interferometer (SSI). The ring-Sagnac has been more extensively developed, and we therefore take it as the reference

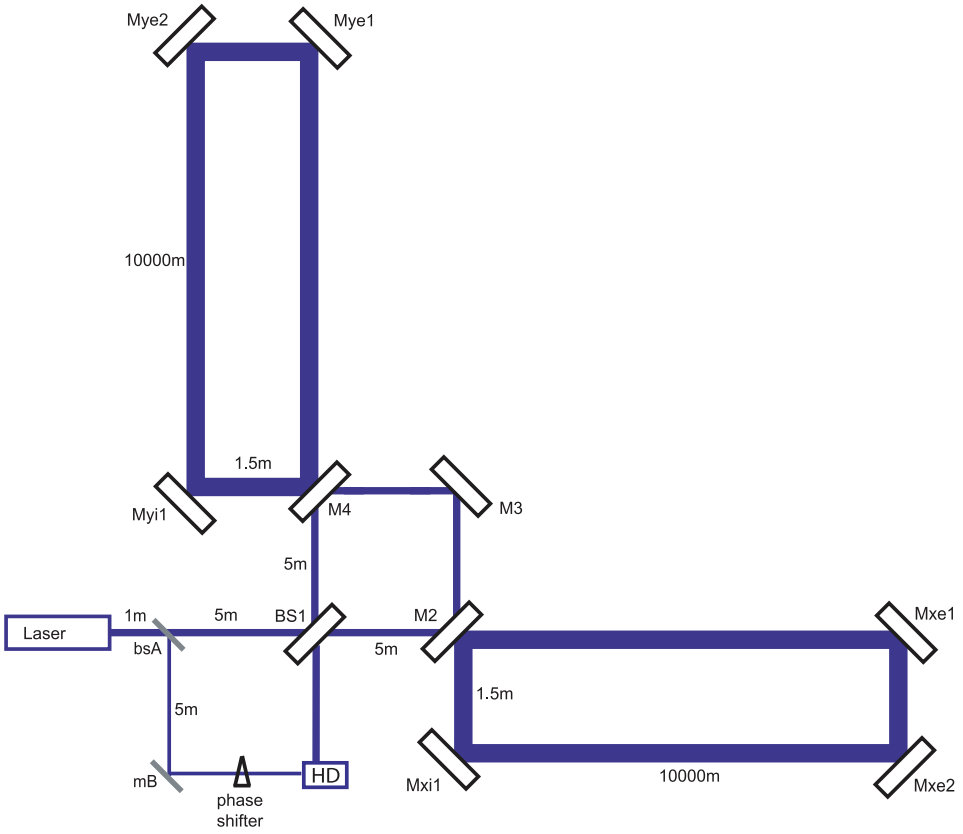

Figure 1. Schematic of ring-Sagnac interferometer. The inner Sagnac interferometer is composed of beamsplitter BS1 and mirrors M2, M3 and M4. M2 and M4 are also the coupling mirrors for the 10 km long arm cavities, of which the remaining mirrors are highly reflective. Light propagates round the inner ring and both arm cavities in both directions. The optics required for homodyne readout (bsA, which splits of a suitable small fraction of the ingoing light, BS1, mB, a phase shifter—simply an adjustable optical path, and the detector HD) are seen on the lower left part of the figure. Further properties of the components are described in section 3.

design. The newer sloshing-Sagnac interferometer was introduced by one of us [19] and has the potential advantage of reducing the coating thermal noise (see section 7). These interferometer configurations are illustrated in simplified form in figures 1 and 2. The designs are described in more detail in sections 3 and 4 respectively.

The ring-Sagnac is a direct development from the zero-area Sagnac interferometer. The primary modification is that a resonant cavity is included in each arm. The finesse of this cavity is chosen to yield the desired storage time for the light for optimal cancellation of the position information from the main signal. The cavity must support clockwise and counter-clockwise propagation of the light around the inner part of the Sagnac interferometer. Two methods of achieving this separation are under consideration. The first of these employs ring cavities [8]. The alternative approach uses polarising optics and linear arm cavities, which allows the counter-propagating beams to be separated according to their polarisation state [9, 11, 12].

In either solution leakage or scattering of light from one light field to the other contaminates the velocity signal by reintroducing sensitivity to mirror position, reducing the potential

suppression of quantum radiation pressure noise. There are technical challenges associated with both methods: e.g. the use of 45-degree incidence within the ring cavities comes at the cost of requiring toric mirrors to maintain good matching of the optical mode. Such mirrors may prove difficult to manufacture with the required quality. In the polarisation method the challenge is to identify polarising optics (polarising beam splitters and wave plates, in particular) with the required quality over a sufficiently large clear aperture. At the level of the simulations presented in this work the two technical approaches to the ring-Sagnac would be expected to perform similarly, provided the storage times of the respective arm cavities were adjusted to be the same.

Practical considerations motivate us to investigate the new sloshing-Sagnac configuration as that approach does not require ring cavities or polarising optics within the main part of the interferometer. Only conventional beam splitters, linear resonant cavities and steering mirrors are required, all of which can be similar to those routinely employed in the existing detectors.

The sloshing-Sagnac interferometer is built around a beam splitter which directs light into two long linear resonant cavities as shown in figure 2. Unlike in conventional designs such as the Advanced LIGO interferometers, all four mirrors forming these cavities have equal reflectance (and transmittance). The system is completed by linking the far ends of the two cavities with a pair of steering mirrors and an additional anti-resonant cavity, as shown. Further refinements of the sloshing-Sagnac design are introduced in section 4.

Although there are many classical sources of noise that must be evaluated as part of the design of a gravitational wave detector, in this paper we consider, primarily, the quantum noise contribution. Quantum noise, by which we mean the combination of shot noise and quantum radiation pressure noise, is expected to be limiting in Advanced LIGO over much of the observing band. Classical noise is continuously being driven down through technical improvements in mirror materials, suspensions etc and we expect that roughly the same level of classical noise would be reached with any of the designs that we compare. The exception to this is coating thermal noise: the sloshing-Sagnac design is specifically intended to reduce this, as considered in section 7.

While analytic expressions for the quantum noise spectra for the configurations of interest have already been derived, these tend to require several simplifying assumptions. With ideal instruments, the energetic quantum limit [10] indicates that practical design features such as optical loss and maximum tolerable light power determine the lowest achievable quantum noise. Evaluation of design options is then a matter of practicality rather than fundamental limits. An aim of our work is to identify and evaluate, in this practical context, implementations of the two speedmeter designs. To optimise and evaluate many options we decided to carry out the work reported here by numerical simulation. The main part of this was performed using FINESSE [20].

Our general aim is to identify the best design option for a future gravitational wave detector. We take the Einstein telescope (ET) design, as a well-studied starting point, and take all the main design parameters from the ET design study [5] as a starting point for our work. We therefore started from ideal versions of the ring- and sloshing-Sagnac interferometers, selected to have as many design parameters as possible taken from ET. We model Gaussian beams and appropriately curved (spherical or toric) mirror surfaces to produce a well mode-matched system. To simulate the opto-mechanical interactions, in which the mirrors are free to move in response to radiation pressure, we model all mirrors suspended as pendulums with a resonant frequency well below the observing band (the precise choice of this frequency does not affect the resulting noise spectra in the observing band as the mirrors behave as free masses at frequencies above the pendulum resonance). The main parameters we copy from the ET design are the mirror-mass of 200 kg, and the 10 km length for the interferometer's arms, intended to fit into an equilateral-triangle vacuum system of 10 km side.

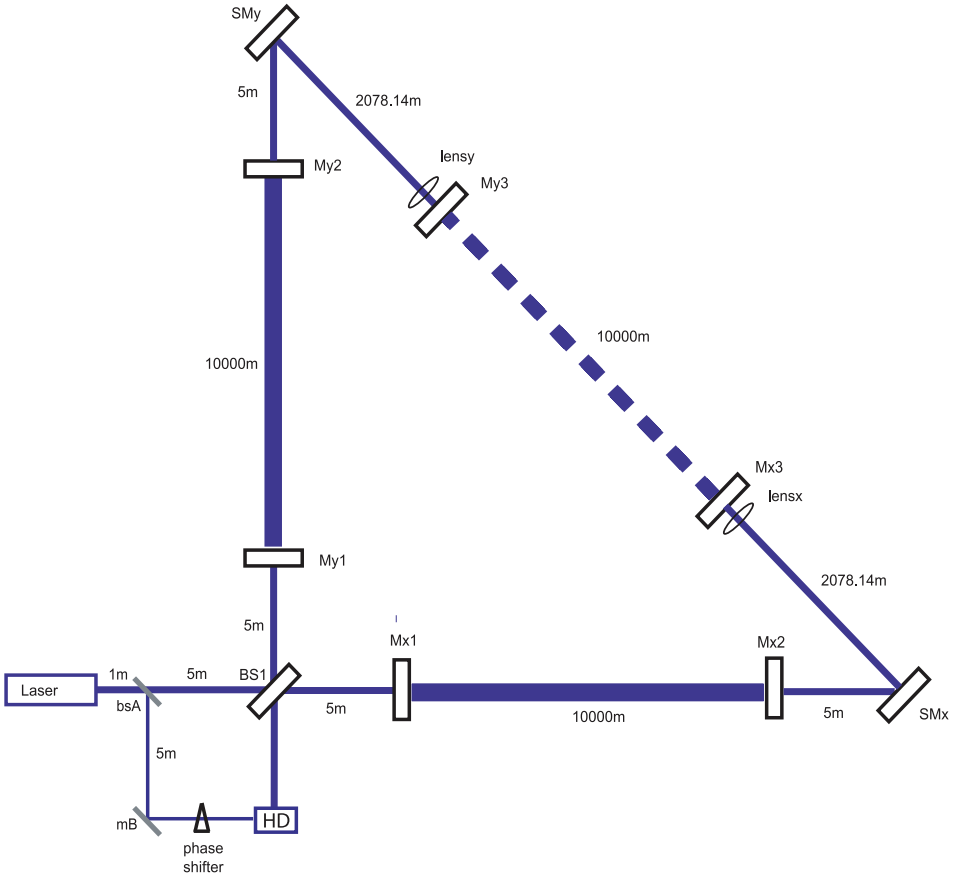

Figure 2. Schematic of the sloshing-Sagnac interferometer. The core interferometer is formed by BS1 and the two arm cavities formed from four mirrors of the same reflectance (Mx1, Mx2, My1, My2). The distant ends of these are linked by an anti-resonant cavity (Mx3, My3). The end test masses of this resonant arm cavities are linked via steering mirrors (SMx, SMy) to a 10 km long anti-resonant cavity. The lenses (lensy, lensx) are required to match the cavity modes and these would most likely be incorporated into the substrates of the adjacent mirrors in a practical implementation. The short linking paths are all 5 m. The optics required for homodyne readout, on the lower left part of the figure, work in the same manner as for the ring-Sagnac. Further properties of the components are described in section 4.

The light power circulating in the arm cavities depends on their finesse and the power coming from the inner part of the interferometer. It is likely that practical interferometers will be limited by the maximum tolerable circulating light power in the arm cavities. This typically sets a limit as a consequence of the absorption of even a small part of the circulating light (typically sub-part-per-million absorption in state of the art mirrors). Absorption leads to unwanted heating, thermal distortion and non-linear behaviour of the interferometer. Once again following the choice taken for an ET interferometer design, we restrict the intra-cavity power to 3 MW. To keep the optical simulations as simple as possible we omitted power recycling which has the effect, in a practical implementation, of significantly reducing the power required from the laser. Its absence has no effect on our results.

After the arm-length and light power are chosen, the next most significant parameter is the finesse of the arm cavities, which must be optimised for each case. Together these determine the interaction time with the gravitational waves.

The final simulation parameters that must be chosen further determine the observing band and shape of the frequency response of the detector. The main advantage of speedmeters, given the design parameters noted above, is expected to be seen in the band below $\sim$100 Hz. We consider the interferometer to be limited by quantum rather than classical noise (i.e. all contributing noise sources apart from quantum noise) above 5 Hz, and we assume that there is no useful sensitivity below this. In order to complete our analysis it was necessary to make several assumptions regarding the probable spectrum of classical noise. We have disregarded all further detail of classical noise except that above 5 Hz it is assumed to lie somewhat below the standard quantum limit up to $\sim$100 Hz and below the expected quantum noise at higher frequencies, such that the potential offered by QND methods can be realised in terms of a more sensitive detector. This has consequences, discussed below, for our approach to optimising the parameters of the speedmeters.

Detection of the signal from an interferometer requires the mixing of the signal-containing light with a stronger beam and here we assume the use of a homodyne detector. Measurement of the resulting field or fields on photo-diodes, with their square-law response to amplitude, yields electronic signals of a suitable magnitude for recording [21, 22]. Homodyne detectors are typically set up to pick out one quadrature of the emergent signal, e.g. the phase or amplitude quadrature. In our case, however, the correlation introduced within the interferometer typically yields the largest signal to noise ratio at frequencies of interest with some intermediate phase for the homodyne field. We decided to search over this parameter to find the optimum value as a function of signal frequency and did so by optimising at 5 Hz intervals in the band from 5 Hz to 100 Hz. We then recorded the corresponding best sensitivity curve, with the optimum homodyne phase then held constant at the chosen value. It turned out that for the designs considered, optimising at a signal frequency of 10 Hz or 15 Hz most often produced the best overall result.

It should be noted that we did not consider the application of squeezing. When this technique is applied, squeezed light, or more precisely, squeezed vacuum generated in an external system of non-linear optics, is employed to reduce the measured quantum noise. While this may result in improved sensitivity, we do not expect that it would be a strong differentiator among the configurations under consideration. This will, however, be studied in future work.

We explicitly state here, that it is not our intention to compare our sensitivity curves with that of ET [5], this study is only intended to show the potential improvements in quantum noise which could be achieved with our speedmeter configurations.

This document is organised as follows: section 2 presents the relevant theory of speedmeter interferometers, necessary to place the numerical results in context. Section 3 introduces the ring-Sagnac interferometer and gives examples of its characteristic sensitivity curve (quantum noise performance). Section 4 does the same for the sloshing-Sagnac interferometer. In section 5 we show how the performance was optimised, first to obtain the strongest suppression of noise below the SQL, and second to yield the best sensitivity ranges for the binary black holes (BBH). Section 6 presents an alternative comparison of sensitivity in which the shot noise contribution at high frequency is kept constant. In section 7 we consider the thermal coating noise contribution. Finally, we present our conclusions in section 8.

2. Quantum noise of a ring-Sagnac and sloshing-Sagnac interferometer

In this section, we perform an analytical study of a quantum noise of the two Sagnac interferometers in question. For the analysis, we use the traditional two-photon formalism,

introduced by Caves and Schumaker for the analysis of quantum fluctuations of precision interferometers in their pioneering works [23, 24].

The electric field strain of a monochromatic electromagnetic wave with a central frequency ω_0 can be characterised at an arbitrary point of the z-axis coinciding with its direction of propagation by its quadrature amplitudes:

$$\hat{E}(x,\, y,\, \zeta = t - z/c) = \mathcal{E}_0 u(x,\, y)[(A_c + \hat{a}_c(\zeta))\cos\omega_0\zeta + (A_s + \hat{a}_s(\zeta))\sin\omega_0\zeta], \tag{1}$$

where $\mathcal{E}_0 = \sqrt{4\pi\hbar\omega_0/(\mathcal{A}c)}$ with $\mathcal{A}$ the cross-section area of the light beam. The factor $u(x,\, y)$ describes the transverse beam structure, which is of no particular influence on the quantum noise and thus can be omitted. Following the standard procedure of linearisation of the optomechanical interaction we separate *sine* and *cosine* quadrature amplitudes into a classical (denoted by capital letters, $A_{c,s}$) and quantum fluctuation (small capped letters, $\hat{a}_{c,s}(t)$) parts. This allows to describe the dynamics of the light field in the interferometer as the transformation of the 2D quadrature vectors:

$$\boldsymbol{A} = \begin{bmatrix} A_c \\ A_s \end{bmatrix}, \quad \text{and} \quad \hat{\boldsymbol{a}} = \begin{bmatrix} \hat{a}_c \\ \hat{a}_s \end{bmatrix}. \tag{2}$$

We are interested mostly in the stationary quantum noise properties, such as its power spectral density, we carry out our calculations with spectra of quantum fluctuations expressed in terms of quadrature amplitude spectra using the Fourier transform as:

$$\hat{a}_{c,s}(t) = \int_{-\infty}^{\infty} \frac{\mathrm{d}\,\Omega}{2\pi}\, \hat{a}_{c,s}(\Omega)\mathrm{e}^{-\mathrm{i}\Omega t}, \tag{3}$$

with $\Omega = \omega - \omega_0$ the sideband frequency. In the following we omit the argument Ω for convenience and clearer presentation.

Using the above, one can immediately write down the input/output relations for any interferometer in a general linear transducer form, that for quadrature amplitudes read:

$$\hat{\boldsymbol{b}}^{\mathrm{out}} = \mathbb{T}\cdot\hat{\boldsymbol{a}}^{\mathrm{in}} + \mathbf{R}_h h/h_{\mathrm{SQL}}, \tag{4}$$

where $\mathbb{T}$ and $\boldsymbol{R}n_h/h_{\mathrm{SQL}}$ stand for the optical and optomechanical transfer matrices of the interferometer, respectively, and

$$h_{\mathrm{SQL}} = \sqrt{\frac{8\hbar}{\mu_{\mathrm{eff}} L^2 \Omega^2}} \tag{5}$$

is the free-mass amplitude spectral density of the standard quantum limit in terms of GW strain for an interferometer with the effective mechanical displacement mode mass μ_{eff} and arms length L.

For the two schemes that we consider in this manuscript, one can write down a particularly concise expression[1] for the transfer matrices:

$$\mathbb{T} = \mathrm{e}^{2\mathrm{i}\beta(\Omega)}\begin{bmatrix} 1 & 0 \\ -\mathcal{K}(\Omega) & 1 \end{bmatrix}, \text{ and } \mathbf{R}_h = \mathrm{e}^{\mathrm{i}\beta(\Omega)}\sqrt{2\mathcal{K}(\Omega)}\begin{bmatrix} 0 \\ 1 \end{bmatrix}, \tag{6}$$

[1] This simplification of input–output relations become possible for the specific case of resonance-tuned arm cavities. In the general case, there is no single optomechanical coupling factor $\mathcal{K}$ that can accumulate all the physics of the optomechanical interaction in the interferometer, and one has to consider the cross-coupling between the sine and cosine quadrature amplitudes happening in the detuned Fabry–Pérot cavities.

where $\mathcal{K}$ is the optomechanical coupling factor first introduced by Kimble *et al* in [7]. Here $\beta(\Omega)$ is the phase shift that the sidebands of the input light, with frequency offset $\Omega = \omega - \omega_0$ with respect to the carrier frequency ω_0, acquire as they propagate through the whole interferometer to the readout point.

For the ring-Sagnac interferometer (RSI), the corresponding expressions are derived in several works [8, 25, 26] and read[2]:

$$\mathcal{K}_{\mathrm{RSI}}(\Omega) = \frac{4\Theta\gamma_{\mathrm{arm}}}{(\Omega^2 + \gamma_{\mathrm{arm}})^2}, \text{ and } \beta_{\mathrm{RSI}}(\Omega) = 2\arctan\frac{\Omega}{\gamma_{\mathrm{arm}}} + \frac{\pi}{2}. \tag{7}$$

where $\Theta = \frac{4\omega_p P_c}{\mu_{\mathrm{eff}} c L}$ is the normalised total light power, P_c, in both arms from both light beams, and $\gamma_{\mathrm{arm}} = cT/(4L)$ is the arm half-bandwidth and T the transmittance of the input coupler. Note that for the ring-Sagnac interferometer the effective mass of the differential mechanical mode is 1/8 of the individual mirror's mass, i.e. $\mu_{\mathrm{eff}} = M/8$.

For the sloshing-Sagnac interferometer (SSI), the similar expressions can be easily obtained, using the I/O-relations formalism and keeping in mind that the effective mass here is two times that of the ring-Sagnac interferometer, i.e. $\mu_{\mathrm{eff}} = M/4$. Here we assume that the arm cavities and the sloshing cavity have the same length L and comprise of identical mirrors with mass M and transmissivity $T = 1 - R$, one can introduce their half-bandwidth as $\gamma_{\mathrm{arm}} = cT/(2L)$, where we took into account that the bandwidth of the critically coupled arm cavities is twice that of the overcoupled ones of the traditional interferometers with a single, relatively high-transmissivity coupling mirror [27]. Then the optomechanical coupling and the sidebands' phase shift in the sloshing-Sagnac interferometer read:

$$\mathcal{K}_{\mathrm{SSI}}(\Omega) = \frac{4\Theta\gamma_{\mathrm{arm}}}{(\gamma_{\mathrm{arm}}^2 - 4\,\Omega^2)^2 + 4\gamma_{\mathrm{arm}}^2\,\Omega^2}, \text{ and } \beta_{\mathrm{SSI}}(\Omega) = \arctan\frac{2\gamma_{\mathrm{arm}}\,\Omega}{\gamma_{\mathrm{arm}}^2 + 4\,\Omega^2} + \frac{\pi}{2}. \tag{8}$$

The readout of the third generation interferometers is most likely to be performed by the balanced homodyne detector (BHD) that allows to measure an arbitrary quadrature of the outgoing light by means of measuring the difference photocurrent, $\hat{i}_\zeta^{\mathrm{out}}$, of the two photodiodes of the BHD where the desired quadrature is chosen by means of changing the relative phase shift ζ between the local oscillator beam and the signal one:

$$\hat{i}_\zeta^{\mathrm{out}} \propto \hat{b}_c^{\mathrm{out}}\cos\zeta + \hat{b}_s^{\mathrm{out}}\sin\zeta \equiv \mathbf{H}_\zeta^{\mathrm{T}}\cdot\hat{\boldsymbol{b}},\ \mathbf{H}_\zeta \equiv \begin{bmatrix}\cos\zeta\\ \sin\zeta\end{bmatrix}. \tag{9}$$

Using this definition of the readout quadrature, the corresponding quantum noise spectral density in the desired units, e.g. in units of GW strain amplitude, can be obtained, using the following simple rule:

$$S^h(\Omega) = h_{\mathrm{SQL}}^2\frac{\mathbf{H}_\zeta^{\mathrm{T}}\cdot\mathbb{T}\cdot\mathbb{S}_a^{\mathrm{in}}\cdot\mathbb{T}^\dagger\cdot\mathbf{H}_\zeta}{|\mathbf{H}_\zeta^{\mathrm{T}}\cdot\mathbf{R}_h|^2}, \tag{10}$$

where $\mathbb{S}_a^{\mathrm{in}}$ is the spectral density matrix of the incident light, with components defined according to:

$$2\pi\delta(\Omega - \Omega')\mathbb{S}_{a,ij}^{\mathrm{in}}(\Omega) \equiv \frac{1}{2}|\,\mathrm{in}\,\rangle\hat{a}_i^{\mathrm{in}}(\Omega)(\hat{a}_j^{\mathrm{in}}(\Omega'))^\dagger + (\hat{a}_j^{\mathrm{in}}(\Omega'))^\dagger\hat{a}_i^{\mathrm{in}}(\Omega)|\mathrm{in}\rangle, \tag{11}$$

[2] Hereinafter we use the approximation of GW wavelength being much larger than any of the characteristic lengths of the interferometer amounting to $\Omega L/c \ll 1$.

where $|\mathrm{in}\rangle$ is the quantum state of the light injected into the dark port of the interferometer and $(i, j) = (c, s)$ (see section 3.3 in [25] for more details). For in this manuscript we restrict ourselves to vacuum field input, i.e. $|\mathrm{in}\rangle \equiv |\mathrm{vac}\rangle$, the input light spectral density takes a simple form $\mathbb{S}^{\mathrm{in}}_{a,ij} = \delta_{ij}$. Hence, using expressions (6) and substituting them into (10), one obtains a particularly concise expression for the quantum noise power spectral density in units of h in the absence of loss:

$$S^h(\Omega) = \frac{h^2_{\mathrm{SQL}}}{2\mathcal{K}} \left[(\mathcal{K} - \cot\zeta)^2 + 1\right]. \tag{12}$$

Analysis of the above expression aiming at finding the optimal homodyne angle that provides the best quantum noise limited sensitivity (QNLS) at a given frequency Ω_0 immediately yields:

$$\cot\zeta_0 = \mathcal{K}(\Omega_0). \tag{13}$$

Substitution of this homodyne angle value into equation (12) and using the expression for $\mathcal{K}(\Omega)$ from equations (7) or (8), produces the QNLS at a given frequency.

Note that the FINESSE software we employed to estimate the performance of speedmeters applies the two-photon formalism to model the quantum noise of a wide range of interferometer configurations.

Numerical simulations provide convenient and rapid simulation of a wide range of interferometers with a range of parameter sets. It is important to compare the numerical results with the analytical model. To this end, we have chosen to compare numerical and analytical results for one instance of the sloshing-Sagnac interferometer. Here the mirrors have a reflectance of 0.950 for the resonant cavities, and a reflectance of 0.960 for the anti-resonant cavity. Our simulations were setup to consider suspended mirrors not included in our analytical result; the curves would not match near the pendulum frequency. We have, therefore, reduced the pendulum frequency by a factor of 0.001 only for the comparison plot shown in figure 3. It can be seen that the curves agree to the resolution with which our plots can be read.

3. Ring-Sagnac interferometer

3.1. Setup of a ring-Sagnac interferometer

A ring-Sagnac interferometer (RSI) model was setup, as a model in FINESSE, to match the primary specifications of the proposed Einstein telescope (ET), i.e. with ring cavities of 10 km length, 200 kg mirrors and optical wavelength of 1064 nm. As noted above, we assumed that there is a limit to the circulating light power in the ring-cavities of 3 MW. The Gaussian beam-waist is in the middle of each arm to allow the mirrors to be of uniform size, shape and mass, resulting in the set of parameters shown in table 1.

To simplify the simulations by avoiding trivial geometrical effects due to non-right angles, we arranged the arm cavity mirrors to be perpendicular to each other, with the interferometer taking the form of a right-angled isosceles triangle, rather than the planned equilateral triangle to fit the infrastructure of ET. This simplification causes no loss of applicability to ET. It was previously found [28] that, for reasons of small-angle scattering when combined with space restrictions within the vacuum envelope, a bow-tie cavity or a triangular ring-cavity are less favourable than a rectangular ring-cavity. We have therefore chosen to model the latter option.

The schematic of the ring-Sagnac interferometer is shown in figure 1. When the light passes through BS1 it enters the inner-Sagnac. The inner-Sagnac consists of the first ring formed by BS1, M2, M3 and M4. The mirrors M2 and M4 are partially transmitting and so act as input

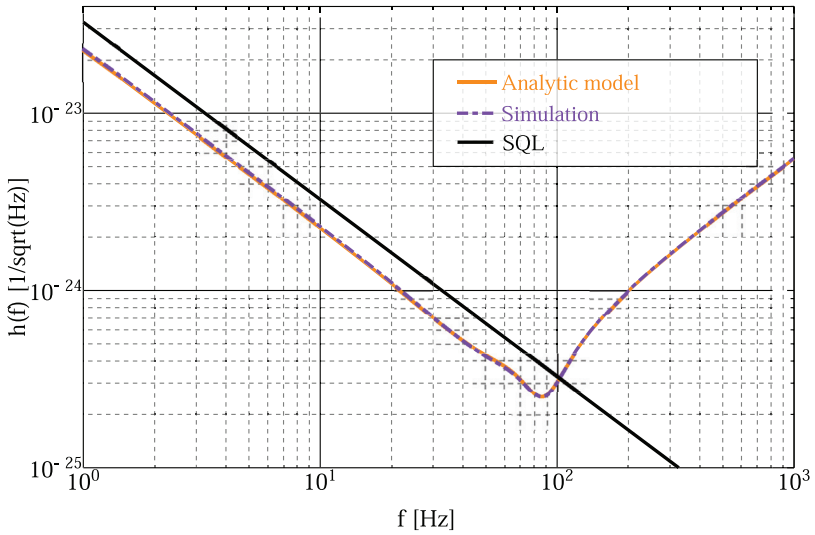

Figure 3. Comparison of the analytical model and the numerical results for the sloshing-Sagnac interferometer. The chosen system has a reflectance of 0.950 for the resonant cavities and of 0.960 for the anti-resonant cavity. The power in the resonant arms is 3 MW. (The simulation uses parameters as specified in figure 2 and table 2; and a reduced pendulum frequency.)

Table 1. Parameters of the ring-Sagnac interferometer. The radii of curvature are chosen for correct mode-matching. Toric mirrors are required in the ring cavities to cancel astigmatic errors. Here Rch labels the horizontal curvature and Rcv the vertical. The reflectance values for the main mirrors are varied to optimise the quantum noise limited curves as described in the text.

Radius of curvature	Rch (m)	Rcv (m)
BS1, bsA, bsB, bsC, HD, M3	∞	∞
M2, M4, Mx.., My..	15 727	7868.5
Reflectivity, loss	R (-)	L (-)
BS1, HD	0.5	0
bsA	0.001	0
M3, Mx.., My..	1	0
M2, M4	Varies	0
Light power	I_c (MW)	
in the resonant arm cavities	3	
Laser wavelength	λ (nm)	
Nd:YAG	1064	

couplers for the ring-cavities in the x- and y-direction. All other mirrors in the inner Sagnac have unit reflectance. We operate the interferometer in homodyne detection as shown, where a part of the incoming light is combined with the light which exits the interferometer at BS1 and detect it at the homodyne detector (HD). The phase of this combination determines the homodyne phase angle.

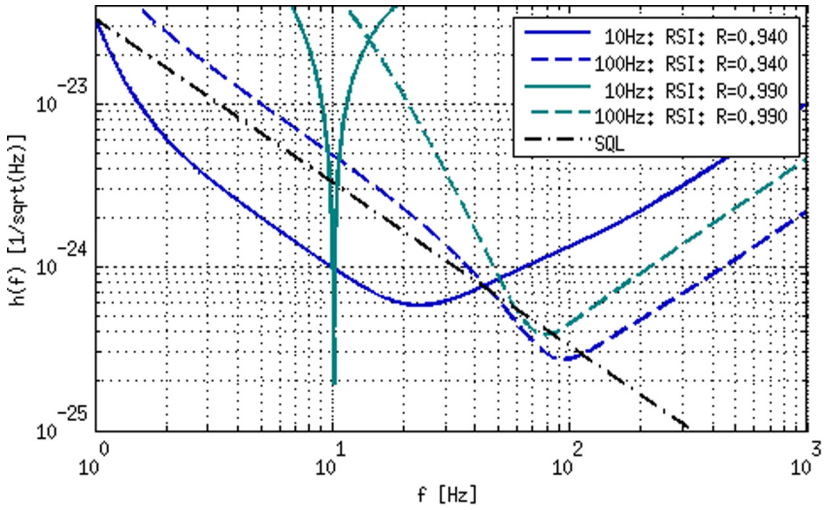

Figure 4. Ring-Sagnac interferometer: quantum noise limited sensitivity curves for two sets of input coupler reflectance ($R = 0.940$ and $R = 0.990$). The homodyne phase is optimised at either 10 Hz or 100 Hz as indicated. The results are discussed in the text.

3.2. Selection of quantum noise limited curves for the ring-Sagnac-interferometer

For a given choice of frequency band within which the system is optimised, the sensitivity of a ring-Sagnac interferometer depends primarily on the reflectance of the input-couplers (M2 and M4)—provided that the homodyne phase is correctly adjusted to suit. Example responses are shown in figure 4 for input coupler reflectance of $R = 0.940$ and $R = 0.990$. To show the effect of homodyne phase we show pairs of results optimised with the phase at 10 Hz and 100 Hz, respectively. These examples illustrate that it is important to have an application in mind before comparing the performance of alternative interferometers in too much detail, and suggests our choice of astrophysically-motivated optimisation.

4. Sloshing-Sagnac interferometer

4.1. Setup of a sloshing-Sagnac interferometer

In the original representation [19], two resonant Fabry–Pérot arm cavities, are arranged in the classical Michelson setup, linked to two anti-resonant Fabry–Pérot cavities of the same length as the main arm cavities and running parallel to them. These anti-resonant cavities are connected to form a Sagnac interferometer, where the light can travel in closed paths, clockwise and anticlockwise, through all four linear cavities. Two particular features of the original representation were that all cavities were critically coupled (i.e. all mirrors were of the same reflectivity), and that each sloshing cavity was set to form, in effect, a Khalili cavity [29]. Khalili cavities, by replacing highly-reflective end mirrors in resonant arm cavities, have the potential advantage of allowing a reduction of the coating thermal noise, and we consider this aspect further in section 7. In this design, counter propagating light fields interfere destructively in the secondary or anti-resonant cavities and turn them into sloshing cavities, leading to the name sloshing-Sagnac interferometer.

Table 2. Parameters of the sloshing-Sagnac interferometer. In this case the mirror-surfaces are spherical. The reflectance of the main mirrors is optimised within the simulation. The mirrors of the anti-resonant cavity may have the same or different reflectance than the mirrors of arm cavities, as described further in the text. (As stated in figure 2, the lenses (lensy, lensx) would most likely be incorporated into the substrates of the adjacent mirrors in a practical implementation).

Radius of curvature	Rc (m)	
BS1, bsA, bsB, bsC, SMx, SMy	∞	
Mx/y1, Mx/y2	5560.4	
Mx/y3	5113.5	
Focal length	f (m)	
lensx/y	3043.3	
Reflectivity, loss	R (-)	L (-)
BS1, HD	0.5	0
bsA	0.001	0
SMx/y	1	0
Mx/y1, Mx/y2, Mx/y3	Varies	0
Light power	I_c (MW)	
in the resonant arm cavities	3	
Laser wavelength	λ (nm)	
Nd:YAG	1064	

In the current work we consider a development and simplification of the sloshing-Sagnac approach: the two resonant cavities are linked by a single anti-resonant sloshing cavity. Thus we have simplified the simulation by reducing the number of cavities, but without losing any fundamental aspects of performance. We further remove the requirement for the mirrors to have the same reflectance as those of the arm cavities. This adds another degree of freedom in the optimisation of the detector's response.

Again, for convenience in modelling, we choose to form the interferometer with the geometry of a right-angle isosceles triangle, without losing applicability to ET. The 10 km-long resonant cavities are placed in the two shorter sides of the triangle and the anti-resonant cavity in the hypotenuse. We choose the same 3 MW circulating power as for the ring-Sagnac. The arrangement is shown in figure 2 with parameters listed in table 2.

4.2. Sensitivity curves for the sloshing-Sagnac-interferometer

The sloshing-Sagnac design presented here permits the finesse of the sloshing cavity to differ from that of the main arm cavities. To determine whether, for example, increasing the finesse of the anti-resonant cavity would be of benefit, the reflectance of its mirrors, Mx3 and My3—taken to be identical, was varied. This was carried out for a range of arm cavity finesse. As an example of the response of the sloshing-Sagnac, we have chosen to show, in figure 5, a set of results all with a reflectance of 0.950 for the resonant cavities and values of 0.960, 0.970, 0.980 and 0.990 for the anti-resonant cavities. All of these curves were optimised, in terms of local oscillator phase, for performance at 10 Hz. It can be seen that the curves have roughly the same broad characteristics and as the finesse of the anti-resonant cavity increases the sensitivity dips further below the SQL. The trade-off is that sensitivity becomes poorer at higher frequencies.

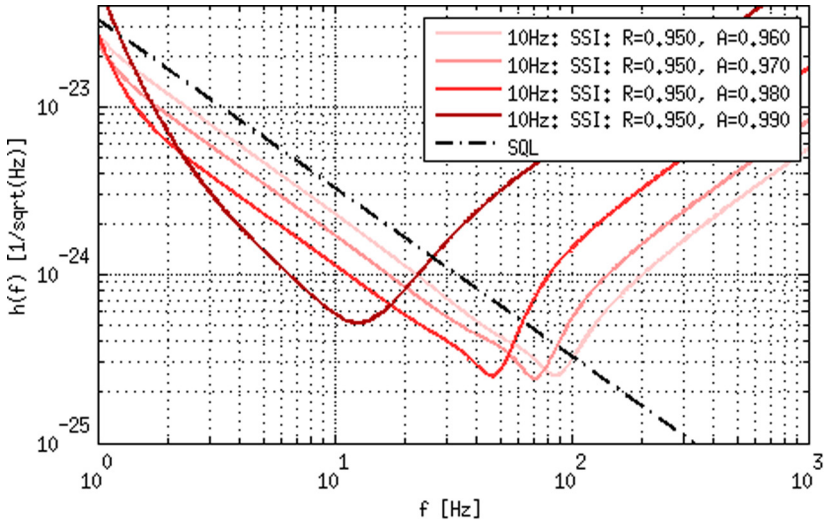

Figure 5. Sloshing-Sagnac interferometer: quantum noise limited sensitivity curves for different reflectances (values A in the legend) of the anti-resonant cavity mirrors. In all cases the reflectance of the four arm-cavity mirrors is $R = 0.950$, the homodyne phase is optimised for best sensitivity at 10 Hz.

5. Methods of optimising and comparing the designs

For both types of interferometer under consideration, the shape of the sensitivity curve is strongly dependent on the set of parameters chosen (i.e. the mirror properties and homodyne phase). To obtain a useful comparison, it is important to evaluate the performance of a potential future gravitational wave detector with respect to astrophysically-motivated goals.

The first approach we take is to maximise the area below SQL, to give a general increase in low frequency performance, as may be appropriate in the case of searching for unmodelled signals. To do this we calculate and maximise the integrated sensitivity improvement.

The second approach is targeted towards optimising the sensitivity for the most-favoured potential signals in the relevant frequency band: those produced by binary black hole (BBH) inspirals. To accomplish this calculation, we make use of existing software and export our FINESSE output files (representing noise power spectral density over the relevant frequency range) into GWINC [30]. The result produced by this code involves weighting the sensitivity curve by $f^{3/7}$, where f is the signal frequency, to represent the frequency dependence of the signal produced during the late-stage inspiral phase of a compact body interaction and integrating over the chosen frequency band. For concreteness, we took as benchmark an equal-mass binary with individual black hole masses of 30 $M_{\odot}$. Optimising for heavier or lighter systems would shift the best-case responses towards lower and higher frequencies, respectively.

To produce the final result by this method, we process our pool of FINESSE output files and inspect the results to find those representing best sensitivity (i.e. longest range of detection for the BBH signal). Since we neglect classical noise the absolute ranges are unrealistically large, and to avoid confusion we present relative ranges for comparison of interferometer designs.

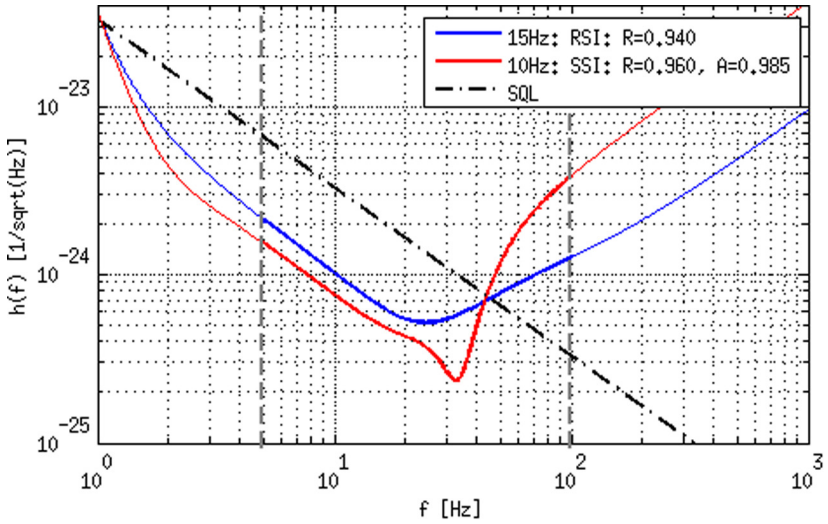

Figure 6. Quantum noise limited sensitivity curves for the different interferometer types which were optimised for the maximum area below the SQL. For this optimisation we have chosen a lower limit of 5 Hz and an upper limit of 100 Hz, which is indicated through dashed the vertical lines. R indicates arm-cavity mirror reflectance, and A the anti-resonant cavity mirror reflectance in the case of the sloshing interferometer. See also table 3.

Table 3. Maximum area below the SQL for the different interferometer types of figure 6. The normalised BBH inspiral ranges are given for information only, and were not used for optimisation in this set of results. Note that the tabulated results are dimensionless. As before, R indicates arm-cavity mirror reflectance, and A the anti-resonant cavity mirror reflectance for the sloshing interferometer.

Interferometer type	Maximum area below the SQL	Normalised inspiral range BBH
RSI (15 Hz, $R = 0.940$)	165.1×10^{-48}	1
SSI (10 Hz, $R = 0.960$, $A = 0.985$)	176.6×10^{-48}	1.44

In both the general low-frequency and BBH-optimised results, we take 5 Hz as the lower limit of the observing band. In section 6 we compare interferometers by a third method in which we match high frequency performance.

5.1. Sensitivity optimised for area below the SQL

We first compare the two interferometer designs in terms of the maximum integrated noise power reduction below the SQL. The optimisation, which includes the best choice of homodyne phase to maximise sensitivity at the frequency noted with each result, was carried out by searching over sufficiently fine grid of parameters. For example, mirror reflectance values were adjusted in steps of 0.005.

Our findings are displayed in figure 6, with numerical results in table 3. With the particular optimisation shown, the sloshing-Sagnac achieves a better reduction of noise below the standard quantum limit, though poorer sensitivity above ∼44 Hz.

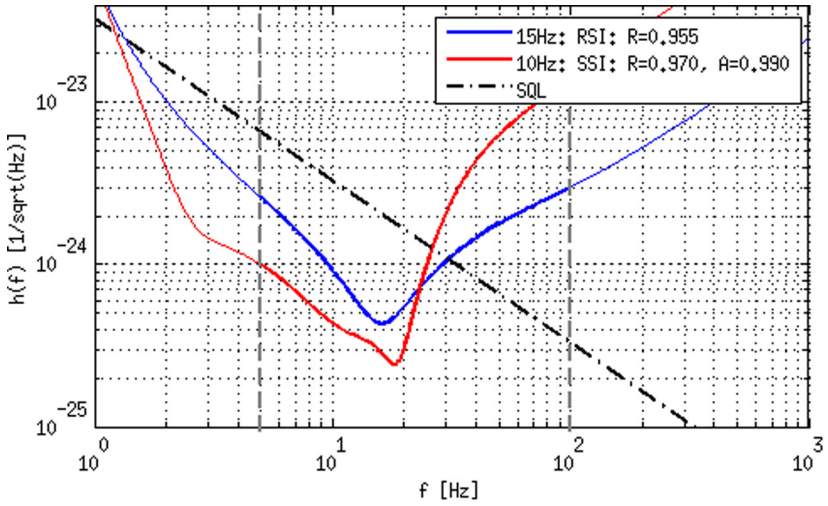

Figure 7. Overall best quantum noise limited sensitivities in respect to the BBH inspiral ranges of our interferometers which were optimised for the frequency range from 5 to 100 Hz. (The range is as before indicated by the dashed vertical lines.) It was found that the ring-Sagnac was best when when optimised at 15 Hz, whereas the sloshing-Sagnac was found to be best when optimised at 10 Hz.

Table 4. Overall 'best' normalised BBH inspiral ranges for the different interferometer types of figure 7. The area below the SQL is given for information only.

Interferometer type	Area below SQL	Normalised BBH inspiral range
RSI (15 Hz, $R = 0.955$)	155.2×10^{-48}	1.08
SSI (10 Hz, $R = 0.970$, $A = 0.990$)	165.9×10^{-48}	1.76

5.2. Optimisation by BBH inspiral range

In this section we consider the best sensitivity in respect of the BBH inspiral range. As already mentioned, the FINESSE output files were read into GWINC which generated the BBH inspiral ranges. The corresponding sensitivity curves are displayed in figure 7 with numerical results in table 4.

6. Quantum noise limited sensitivity with matched shot noise

A third comparison of interferometer performance was carried out with the constraint that the two speedmeter designs should have the same shot noise contribution at high frequency. For concreteness, we set the noise to be similar in the frequency band from 500 Hz to 1 kHz. The range of interest is then from 5 Hz to 1 kHz. Response at higher frequencies is useful for wide-band searches, e.g. for neutron-star inspirals or for unmodelled signals.

We started by taking the ring-Sagnac which gave the best area below the SQL as a reference. We then identified a sloshing-Sagnac design that overlapped best at high frequency and with the same optimisation frequency (15 Hz). Figure 8 shows the result and table 5 indicates that

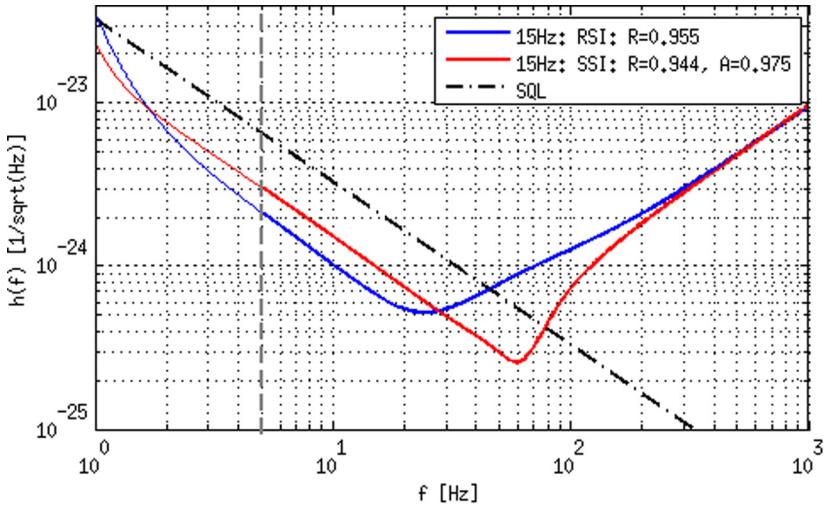

Figure 8. Quantum noise limited sensitivity for the same shot noise contribution for the different interferometer types whereby the sensitivity of the ring-Sagnac with the best area (figure 6/table 3) was taken as a reference. The sloshing-Sagnac was optimised so that the high frequency part overlaps with that of the ring-Sagnac. The vertical dashed line indicates that only frequencies above 5 Hz are considered.

Table 5. Area below the SQL, normalised BBH inspiral ranges for the different interferometer types of figure 8.

Interferometer type	Area below SQL	Normalised BBH inspiral range
RSI (15 Hz, $R = 0.940$)	165.1×10^{-48}	1.13
SSI (15 Hz, $R = 0.944$, $A = 0.975$)	156.5×10^{-48}	1.08

the sloshing-Sagnac approaches but does not quite reach the sensitivity of the ring-Sagnac, by either of our measures.

In a second comparison of this kind, we take the best, sub-SQL optimised, sloshing-Sagnac as reference and match the ring-Sagnac design to it at high frequency: see figure 9. Since the sloshing-Sagnac was optimised for a detection frequency of 10 Hz, we chose the same optimisation frequency for the ring-Sagnac. In this case the sloshing-Sagnac has a better performance than the ring-Sagnac, by both measures, as can be seen in table 6.

These last two plots above illustrate the difficulty of comparing interferometer designs when the shape of response differs. When we took the response of the ring-Sagnac as reference, the ring-Sagnac was better than the sloshing-Sagnac. On the other hand, when we took the sloshing-Sagnac as reference, it out-performed the ring-Sagnac, significantly.

7. Coating noise reduction in a sloshing-Sagnac interferometer

We have noted that one motivation for the sloshing-Sagnac design was to reduce the contribution of coating thermal noise by finding a design that did not require maximally reflective mirrors (as typically used as end mirrors, as for example in Advanced LIGO, or for three of the four mirrors in each arm of the ring-Sagnac interferometer). In this section we show that

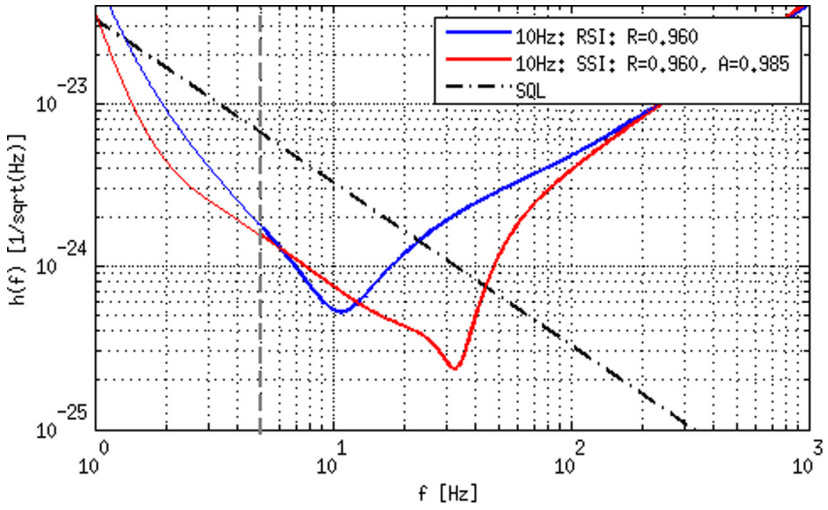

Figure 9. Quantum noise limited sensitivity for the same shot noise contribution for the different interferometer types, whereby the sensitivity of the sloshing-Sagnac with the best area (figure 6/table 3) was taken as a reference. The parameters of the ring-Sagnac Sagnac were chosen so that the high frequency part overlaps with that of the sloshing-Sagnac. Again only frequencies higher than 5 Hz, indicated by the vertical dashed line, are considered.

Table 6. Area below the SQL and the normalised BBH inspiral range for the different interferometer types of figure 9.

Interferometer type	Area below SQL	Normalised BBH inspiral range
RSI (10 Hz, $R = 0.960$)	150.2×10^{-48}	1.24
SSI (10 Hz, $R = 0.960$, $A = 0.985$)	176.4×10^{-48}	1.61

the total coating noise of a sloshing-Sagnac interferometer is indeed smaller than that of a conventional Michelson-interferometer, such as Advanced LIGO.

The relatively simple model we employ here is intended to show, in general terms, the potential reduction in total coating noise that may be obtained using the sloshing-Sagnac configuration. In the process of specifying, in detail, the mirrors of an actual interferometer, a more in-depth analysis of the coating design would be required. At that point a precise calculation of the thermal noise, for instance following the method given in [31], would be appropriate, and this may give slightly different factors of improvement depending on the precise choice of mirror parameters and coating materials.

For this calculation we make a model of the total coating noise, making the assumption that every layer in a coating contributes equally according only to the intrinsic mechanical loss of its material, and that the noise generated in each layer (of every mirror) is uncorrelated with that from the other layers and mirrors. We also neglect the coating noise from all components other than the mirrors of main (resonant) arm cavities. This last assumption is justified by modelling which shows that motion of these components (mirrors other than that of the main arm cavities) contributes relatively weakly to the interferometer's output signal.

The reflectances of the individual arm cavity mirrors are known for conventional designs: e.g. for Advanced LIGO the ITMs (the coupling mirrors) transmit 1.4% while the ETMs (end mirrors) transmit 5 ppm [1]). Based on the results in previous sections of this work, we estimate that a sloshing-Sagnac design could employ cavity mirrors all of which have a reflectance of around 96%—see figure 6 and table 3 and the other examples.

We estimate the required number of coating layers to achieve the various reflectance values required by using the following equation [32] which models standard 1/4-wave multi-layer silica-tantala coatings:

$$R(N) = \sqrt{1 - 2.8 \times 0.49^N} \quad \text{for} \quad N \geqslant 3. \tag{14}$$

Here R is the reflectance of a mirror with N layers of tantala and $(N-1)$ layers of silica. This gives us for the Advanced LIGO cavities mirrors 6 and 18 silica layers, respectively and for our sloshing-Sagnac 6 silica layers per mirror.

As the thermal noise from separate layers is uncorrelated, we add the root mean square contributions of the individual layers of the two pairs of mirrors per interferometer:

$$N_{\text{coat}} = \sqrt{2 \times (N_{m1}^2 + N_{m2}^2)}\,, \tag{15}$$

where N_{m1} and N_{m2} are the silica layers of mirror $m1$ and $m2$.

We can then calculate the amount by which the sloshing-Sagnac's coating noise is reduced compared to that in an Advanced LIGO interferometer. This reduction factor is given by:

$$\Delta = \frac{N_{\text{coat}}(\text{Adv. LIGO})}{N_{\text{coat}}(\text{SSI})} \approx 2.2 \tag{16}$$

In conclusion, due to the lower reflectance required for the resonant (arm) cavity mirrors of the sloshing-Sagnac, compared to the standard Advanced LIGO configuration, the sloshing-Sagnac can not only reduce quantum noise, but also offers a significant reduction of coating noise.

8. Conclusion

We have introduced and analysed a novel sloshing-Sagnac interferometer which is of potential interest for third generation gravitational wave detectors. The study and development of the sloshing-Sagnac interferometer is at an early stage, but our results in respect of its potential sensitivity are promising. In comparison to the longer-established ring-Sagnac, the sloshing-Sagnac achieves similar or in most cases better performance across a range of optimisations. This is in part due to the possibility of choosing the finesse of the sloshing cavity separately from that of the arm cavities, yielding an extra degree of freedom for optimisation. We expect these benefits to remain significant in the presence of classical noise.

At the time of writing no control scheme has been developed for the sloshing-Sagnac design and many other practical considerations require investigation. The promising sensitivity and potential to employ simple linear cavities avoiding major technical challenges associated with alternative designs encourages future development. To this end a design study towards a sloshing-Sagnac interferometer is underway for implementation at the 10 m prototype in Glasgow.

Acknowledgments

The authors would like the thank the Science and Technology Facilities Council (ST/L000946/1), the European Research Council (ERC-2012-StG: 307245) and the University of Glasgow for support for our work, and colleagues within the Institute for Gravitational Research at Glasgow and the LSC for useful discussions.

References

[1] Aasi J *et al* 2015 *Class. Quantum Grav.* **32** 074001
[2] Acernese F *et al* 2015 *Class. Quantum Grav.* **32** 024001
[3] Aso Y *et al* 2013 *Phys. Rev.* D **88** 043007
[4] Abbott B P *et al* 2016 *Phys. Rev. Lett.* **116** 061102
[5] Abernathy M *et al* 2011 www.et-gw.eu/etdsdocument
[6] Braginsky V B and Khalili F J 1990 *Phys. Lett.* A **147** 251
[7] Kimble H *et al* 2002 *Phys. Rev.* D **65** 022002
[8] Chen Y 2003 *Phys. Rev.* D **67** 122004
[9] Danilishin S L 2004 *Phys. Rev.* D **69** 102003
[10] Braginsky V B *et al* 1999 arxiv.org/abs/gr-qc/9907057
[11] Wade A R *et al* 2012 *Phys. Rev.* D **86** 062001
[12] Wang M *et al* 2013 *Phys. Rev.* D **87** 096008
[13] Braginsky V B *et al* 2000 *Phys. Rev.* D **61** 044002
[14] Purdue P 2002 *Phys. Rev.* D **66** 022001
[15] Purdue P and Chen Y 2002 *Phys. Rev.* D **66** 122004
[16] Shaddock D A *et al* 1998 *Appl. Opt.* **37** 7995
[17] Beyersdorf P T *et al* 1999 *Opt. Lett.* **24** 1112
[18] Gräf C *et al* 2014 *Class. Quantum Grav.* **31** 215009
[19] Danilishin S L 2010 http://gw.icrr.u-tokyo.ac.jp/gwadw2010/program/2010_GWADW_Danilishin.pdf
[20] www.gwoptics.org/finesse/
[21] McKenzie M *et al* 2002 *Phsy. Rev. Lett.* **88** 231102
[22] Vahlbruch H *et al* 2006 *Phys. Rev. Lett.* **97** 011101
[23] Caves C and Schumaker B 1985 *Phys. Rev.* A **31** 3068
[24] Schumaker B and Caves C 1985 *Phys. Rev.* A **31** 3093
[25] Danilishin S L and Khalili F Y 2012 *Living Rev. Relativ.* **15** 5
[26] Danilishin S L *et al* 2015 *New J. Phys.* **17** 043031
[27] Freise A and Strain K A 2010 *Living Rev. Relativ.* **13** 1
[28] Pascucci D *et al* in preperation
[29] Khalili F Y 2005 *Phys. Lett.* A **334** 67
[30] https://awiki.ligo-wa.caltech.edu/aLIGO/GWINC
[31] Hong T *et al* 2013 *Phys. Rev.* D **87** 082001
[32] Somiya K 2009 personal communication